ABAQUS implementation of a coupled deformation - hydrogen diffusion - phase field fracture scheme

Emilio Martínez-Pañeda[a,*]

[a] *Department of Engineering, Cambridge University, CB2 1PZ Cambridge, UK*

Abstract

Documentation that accompanies the file `PhaseFieldH.for`, a user element (UEL) subroutine for implementing in Abaqus the coupled deformation - hydrogen transport - phase field fracture scheme proposed by Martínez-Pañeda et al. [1]. A input file is also provided for demonstration purposes. If using this code for research or industrial purposes, please cite:

E. Martínez-Pañeda, A. Golahmar, C.F. Niordson. A phase field formulation for hydrogen assisted cracking. Computer Methods in Applied Mechanics and Engineering 342: 742-761 (2018)

Note that a separate folder can be downloaded at www.empaneda.com/codes for the Abaqus implementation of the phase field fracture method in the absence of hydrogen.

Keywords:
ABAQUS, Phase field, Fracture, Hydrogen embrittlement, Finite element analysis

1. Introduction

The phase field method for fracture [2–4] enjoys great popularity due to its robustness and ability to model interactions and branching of cracks of arbitrary topological complexity [5–7]. The method builds upon: (1) the work by Griffith; crack growth will take place if a critical energy release rate is

*Corresponding author. Tel: +44 1223 7 48525.
Email address: `mail@empaneda.com` (Emilio Martínez-Pañeda)

attained, and (2) continuum damage mechanics; the phase field acts as damage variable, going from 0 (intact) to 1 (fully cracked). The method holds great potential for the modelling of hydrogen assisted cracking, a field where cohesive zone models have been traditionally favoured (see, e.g., [8, 9]). The phase field model could also be of important use in industrial applications, by allowing to address modelling challenges such as mixed mode cracking, complex distribution of initiation sites or interacting cracks. The micromechanisms of hydrogen damage can be easily incorporated into the phase field framework. The model is particularly well suited to account for the bonding strength (fracture energy) reduction caused by hydrogen, as observed in first principles calculations [1, 10].

We provide an efficient and robust implementation of the phase field method in the commercial finite element package ABAQUS. The model also captures hydrogen transport by means of an extended version of Fick's law. Thus, the files could also be useful for those wanting to implement mass diffusion schemes in ABAQUS. An introduction into the phase field method and the hydrogen-dependent phase field formulation presented in [1] is first shown. Those interested in reading exclusively about the usage of the files provided should jump to Section 3.

2. Numerical model

Hydrogen transport towards the fracture process zone and subsequent cracking are investigated by means of a coupled mechanical-diffusion-phase field finite element framework. Section 2.1 describes the hydrogen-dependent phase field formulation, Section 2.2 provides details of the stress-assisted impurity diffusion scheme, and Section 2.3 outlines the general assemblage and implementation.

The formulation presented in this section refers to the response of a solid body Ω with external surface $\partial\Omega$ of outward normal $\boldsymbol{n}$ - see Fig. 1. With respect to the displacement field $\boldsymbol{u}$, the outer surface of the body is decomposed into a part $\partial\Omega_u$, where the displacement is prescribed by Dirichlet-type boundary conditions, and a part $\partial\Omega_h$, where the traction $\boldsymbol{h}$ is prescribed by Neumann-type boundary conditions (see Fig. 1a). A body force field per unit volume $\mathbf{b}$ can also be prescribed. Conversely, no external loading is considered corresponding to the fracture phase field ϕ, driven by the displacement

field of the solid. A Dirichlet type boundary condition can be prescribed at Γ, a given sharp crack surface inside the solid (see Fig. 1b). With respect to the hydrogen concentration C, the external surface consists of two parts (see Fig. 1c): $\partial\Omega_q$, where the hydrogen flux $\boldsymbol{J}$ is known (Neumann-type boundary conditions), and $\partial\Omega_C$, where the hydrogen concentration is prescribed (Dirichlet-type boundary conditions).

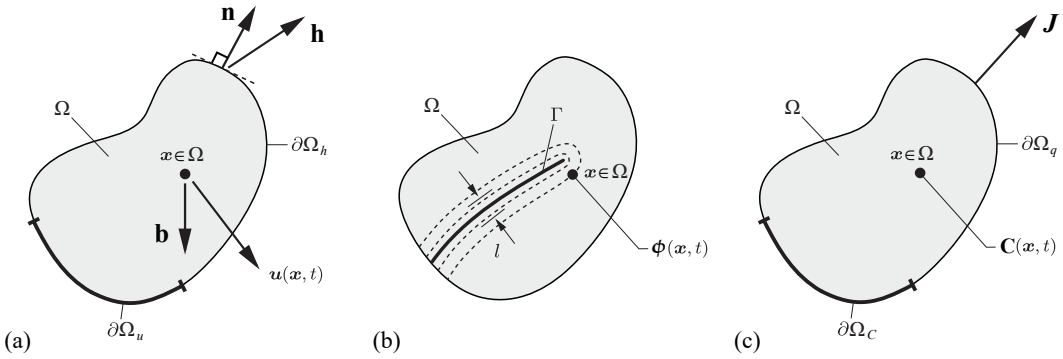

Figure 1: Schematic representation of the three-field boundary value problem: (a) deformation, (b) phase field, and (c) mass transport.

2.1. A phase field formulation for hydrogen embrittlement

2.1.1. Phase field approximation of crack topology

In a one-dimensional setting, the topology of a sharp crack (see Fig. 2a) can be described by an auxiliary field variable $\phi(x) \in [0, 1]$ with

$$\phi(x) = \begin{cases} 1 & \text{if } x = 0 \\ 0 & \text{if } x \neq 0 \end{cases} \tag{1}$$

which is referred to as the crack phase field order parameter, with $\phi = 0$ and $\phi = 1$ respectively denoting the intact and fully broken states of the material. The non-smooth crack phase field (1) can be approximated by the exponential function,

$$\phi(x) = \mathrm{e}^{-\frac{|x|}{\ell}} \tag{2}$$

representing a regularized or diffusive crack topology, as illustrated in Fig. 2b. The length-scale parameter ℓ determines the width of the smearing function, approaching the discrete crack topology as $\ell \to 0$.

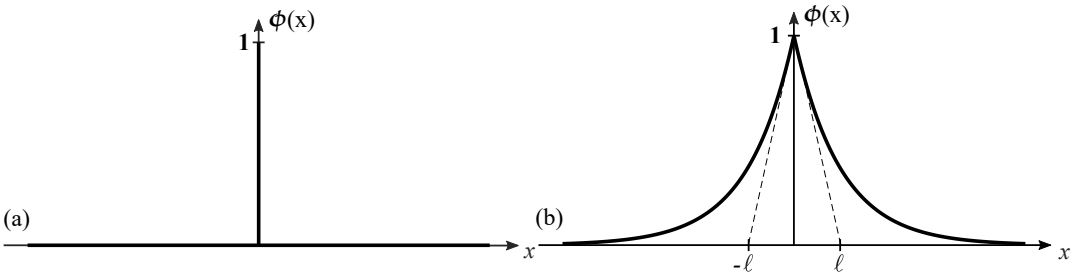

Figure 2: Sharp (a) and diffusive (b) crack topologies.

Consider a discrete internal discontinuity Γ in a solid body Ω (Fig. 3a). A regularized crack functional Γ_ℓ can be defined, in terms of the crack surface density function γ_ℓ, as (Fig. 3b)

$$\Gamma_\ell(\phi) = \int_\Omega \left(\frac{1}{2\ell}\phi^2 + \frac{\ell}{2}|\nabla\phi|^2 \right) \mathrm{d}V = \int_\Omega \gamma_\ell(\phi, \nabla\phi)\, \mathrm{d}V \tag{3}$$

This crack functional Γ-converges to the functional of the discrete crack surface for a vanishing length scale parameter $\ell \to 0$. This is the key point of the phase field method and it has been proven for a continuum medium [11] and for a discrete medium [12]; $\Gamma_{\ell,h}$ converges to Γ for $\ell \to 0$ if $h << \ell$, with h being the mesh spacing. Consequently, the phase field method for fracture circumvents numerical complications inherent to tracking the evolving discontinuity boundary Γ, enabling to robustly model interactions and branching of cracks of arbitrary topological complexity [6]. The fracture energy due to the formation of a crack is then approximated as,

$$\int_\Gamma G_c\,(\theta)\, \mathrm{d}S \approx \int_\Omega G_c\,(\theta) \left(\frac{1}{2\ell}\phi^2 + \frac{\ell}{2}|\nabla\phi|^2 \right) \mathrm{d}V \tag{4}$$

where G_c is the critical Griffith-type energy release rate, which is dependent on the hydrogen coverage θ.

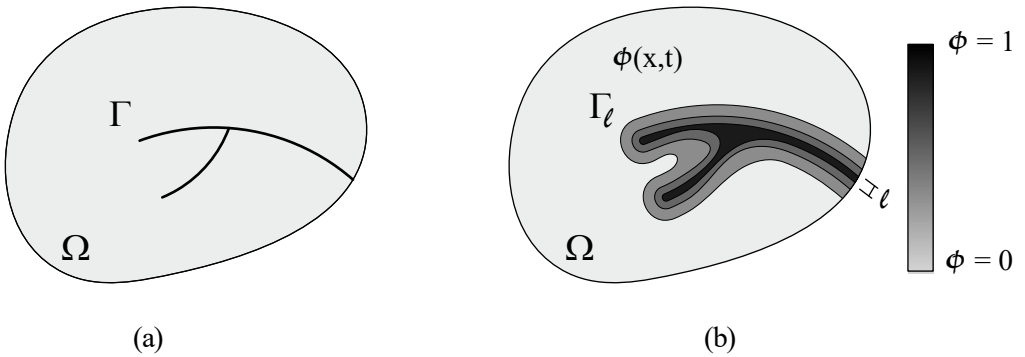

Figure 3: Schematic representation of a solid body with (a) internal discontinuity boundaries, and (b) a phase field approximation of the discrete discontinuities. Adapted from [6].

2.1.2. Governing balance equations

The total potential energy functional of the solid is defined as a function of the displacement $\mathbf{u}$ and the fracture phase field ϕ,

$$\Psi(\mathbf{u}, \phi) = \Psi^b(\mathbf{u}, \phi) + \Psi^s(\phi) \tag{5}$$

where the first term is the stored bulk energy and the last term refers to the surface energy associated with the formation of a crack. The stored bulk energy is given by,

$$\Psi^b(\mathbf{u}, \phi) = \int_\Omega \psi\left(\boldsymbol{\epsilon}(\mathbf{u}), \phi\right) \, \mathrm{d}V = \int_\Omega g(\phi)\psi_0(\boldsymbol{\epsilon}) \, \mathrm{d}V \tag{6}$$

with the function ψ describing the stored bulk energy of the solid per unit volume; ψ_0 denotes the elastic strain energy density for the undamaged isotropic solid,

$$\psi_0(\boldsymbol{\epsilon}) = \frac{1}{2}\boldsymbol{\epsilon}^T : \mathbf{C_0} : \boldsymbol{\epsilon} \tag{7}$$

with $\mathbf{C}_0$ being the linear elastic stiffness matrix. Linear elasticity is assumed here for simplicity but the extension to J2 plasticity is straightforward and can be provided upon request. Additionally, one should note that a linear elastic description of crack tip stresses is closer to the predictions of implicitly multi-scale plasticity formulations (e.g., strain gradient plasticity) than conventional plasticity [13, 14]. We assume small strains and define the strain tensor as,

$$\boldsymbol{\epsilon} = \frac{1}{2}\left[\nabla^T\mathbf{u} + \nabla\mathbf{u}\right] \tag{8}$$

The monotonically decreasing function $g(\phi)$ describes the degradation of the stored bulk energy due to damage evolution. Here we choose a parabolic degradation function,

$$g(\phi) = (1-\phi)^2 + k \tag{9}$$

where k is a parameter chosen to be as small as possible to keep the system of equations well-conditioned; a value of $k = 1 \times 10^{-7}$ is chosen throughout this work.

On the other hand, the fracture energy due to the formation of a crack can be written as

$$\Psi^s(\phi) = \int_\Omega G_c\left(\theta\right) \gamma_\ell(\phi, \nabla\phi)\, \mathrm{d}V \tag{10}$$

where G_c is the critical Griffith-type energy release rate, which is dependent on the hydrogen coverage θ. The total potential energy functional then reads,

$$\Psi(\phi, \mathbf{u}) = \int_\Omega \left\{ \left[(1-\phi)^2 + k\right] H + G_c\left(\theta\right) \left[\frac{1}{2\ell}\phi^2 + \frac{\ell}{2}|\nabla\phi|^2\right] \right\} \mathrm{d}V \tag{11}$$

where we have introduced the so-called history variable field H to ensure irreversibility,

$$H = \begin{cases} \psi_0(\boldsymbol{\epsilon}) & \text{if } \psi_0(\boldsymbol{\epsilon}) > H_t \\ H_t & \text{otherwise} \end{cases} \tag{12}$$

Here, H_t is the previously calculated energy at time increment t. Thus, the history field satisfies the Kuhn-Tucker conditions.

The weak form can be readily computed from the variation of the total potential energy of the solid (11) and the potential energy of the external loading system. Decomposing into the deformation and phase field contributions,

$$\begin{gathered} \int_\Omega \left[g\left(\phi\right) \boldsymbol{\sigma}_0 : \delta\boldsymbol{\epsilon} - \mathbf{b}\cdot\delta\mathbf{u}\right] \mathrm{d}V - \int_{\partial\Omega_h} \mathbf{h}\cdot\delta\mathbf{u}\, \mathrm{d}A = 0 \\ \int_\Omega \left\{ -2(1-\phi)\delta\phi\psi_0(\boldsymbol{\epsilon}) + G_c\left(\theta\right) \left[\frac{1}{\ell}\phi\delta\phi + \ell\nabla\phi\cdot\nabla\delta\phi\right] \right\} \mathrm{d}V = 0 \end{gathered} \tag{13}$$

where $\boldsymbol{\sigma}_0$ is the Cauchy stress tensor of the undamaged solid. Upon making use of the product rule and Gauss' divergence theorem the two sets of

equilibrium equations in Ω can be readily obtained,

$$\begin{aligned} \mathrm{Div}\left[g\left(\phi\right)\boldsymbol{\sigma}_0\right] + \mathbf{b} &= \mathbf{0} \\ G_c\left(\theta\right)\left[\frac{1}{\ell}\phi - \ell\Delta\phi\right] - 2(1-\phi)\,H &= 0 \end{aligned} \tag{14}$$

2.1.3. Hydrogen-dependent surface energy degradation

Hydrogen embrittles metallic materials by lowering the bond energy between metal atoms, which translates into a reduction of the fracture resistance. A number of authors have employed Density Functional Theory (DFT) to investigate the decohesion of fracture surfaces with varying hydrogen coverage (see, e.g., [15–17] and references therein). For example, Alvaro et al. [16] computed the change in ideal fracture energy in the presence of hydrogen atoms at $\Sigma 3$ and $\Sigma 5$ grain boundaries in nickel. Their results, in terms of normalized surface energy $\gamma\left(\theta\right)/\gamma\left(0\right)$ versus hydrogen coverage θ, are shown in Fig. 4, along with a linear fit to the data.

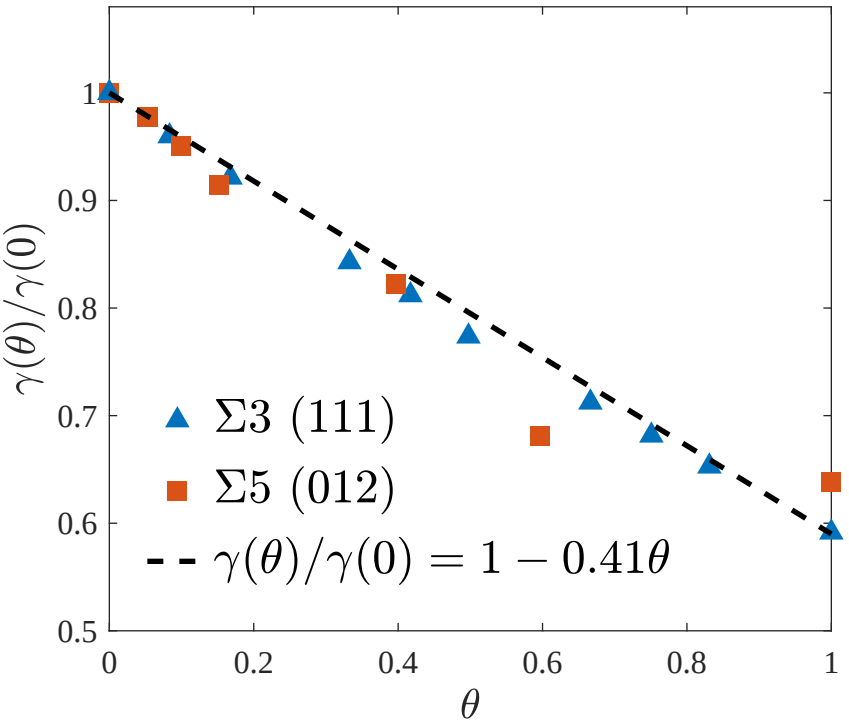

Figure 4: Effect of hydrogen on the surface energy of nickel. Linear fit to the DFT calculations by Alvaro et al. [16] for $\Sigma 3$ and $\Sigma 5$ grain boundaries.

Equivalently, one can define the critical energy release rate dependence on the hydrogen coverage as,

$$\frac{G_c(\theta)}{G_c(0)} = 1 - \chi\theta \tag{15}$$

where $G_c(0)$ is the critical energy release rate in the absence of hydrogen and χ is the damage coefficient that weights the hydrogen-lowering of the fracture energy. χ can be estimated for other materials by fitting DFT data from the literature. The damage coefficient for iron and aluminum is obtained from the work by Jiang and Carter [15] - see Table 1.

Table 1: Weighting factor estimation from first principles quantum mechanics.

Material	Damage coefficient χ	DFT analysis
Iron	0.89	Jiang and Carter (2004) [15]
Nickel	0.41	Alvaro et al. (2015) [16]
Aluminum	0.67	Jiang and Carter (2004) [15]

The effect of hydrogen on the fracture resistance can be illustrated by examining the analytical homogeneous solution of a one-dimensional quasi-static problem. Under these circumstances, the stress is given by $\sigma = g(\phi)E\epsilon$, where E denotes Young's modulus. Given a strain energy density $\psi_0 = E\epsilon^2/2$, one can readily obtain the homogeneous phase field from the strong form (14),

$$\phi = \frac{E\epsilon^2\ell}{G_c\left(\theta\right) + E\epsilon^2\ell} \tag{16}$$

and substituting into the constitutive equation renders the characteristic relation between the homogeneous strain and the homogeneous stress,

$$\sigma = \left(\frac{G_c\left(\theta\right)}{G_c\left(\theta\right) + E\varepsilon^2\ell}\right)^2 E\varepsilon \tag{17}$$

The homogeneous solution for the stress reaches a maximum at a critical stress quantity,

$$\sigma_c = \sqrt{\frac{27EG_c\left(\theta\right)}{256\ell}} \tag{18}$$

with the strain counterpart given by,

$$\epsilon_c = \sqrt{\frac{G_c\left(\theta\right)}{3\ell E}} \tag{19}$$

From (18) an analogy with cohesive zone formulations can be established. Thus, ℓ may be interpreted as a material parameter, which governs the magnitude of the critical stress at which damage initiates. With this in mind, it is interesting to note that, in order to resolve the fracture process zone in a cohesive zone model, the characteristic element size h is typically chosen according to,

$$h < \frac{\pi}{160}\frac{EG_c}{\sigma_c^2} \tag{20}$$

implying that h should be at least 5.4 times smaller than ℓ in the phase field problem. The constitutive relation of the homogeneous phase field problem is shown in Fig. 5 as a function of hydrogen coverage.

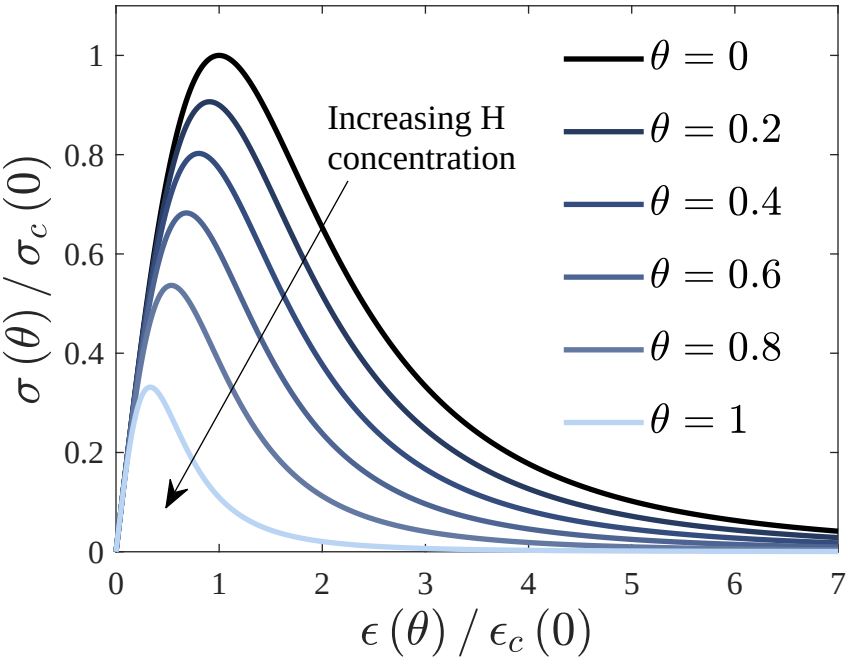

Figure 5: Effect of hydrogen coverage θ on the damage constitutive law for iron-based materials. The stress-strain response is normalized by the corresponding $\theta = 0$ quantities.

As shown in Fig. 5 for the case of iron, hydrogen significantly degrades the strength and the fracture resistance. The present modeling framework quantitatively accounts for the sensitivity of the surface energy to hydrogen coverage, as observed in first principles calculations; other mechanisms of hydrogen damage can also be incorporated.

Finally, we use the Langmuir-McLean isotherm to compute the surface coverage from the bulk hydrogen concentration C,

$$\theta = \frac{C}{C + \exp\left(\frac{-\Delta g_b^0}{RT}\right)} \tag{21}$$

with C given in units of impurity mole fraction. Here, R is the universal gas constant, T the temperature and Δg_b^0 is the Gibbs free energy difference between the decohering interface and the surrounding material. As in [8], a value of 30 kJ/mol is assigned to Δg_b^0 based on the spectrum of experimental data available for the trapping energy at grain boundaries. Thus, the present formulation accounts for the effect of microstructural traps on cracking and can incorporate the influence on mass transport through an effective diffusion coefficient.

2.2. Transport of diluted species

Mass conservation requirements relate the rate of change of the hydrogen concentration C with the hydrogen flux through the external surface,

$$\int_\Omega \frac{dC}{dt}\,\mathrm{d}V + \int_{\partial\Omega} \boldsymbol{J}\cdot\boldsymbol{n}\,\mathrm{d}S = 0 \tag{22}$$

The strong form of the balance equation can be readily obtained by making use of the divergence theorem and noting that the expression must hold for any arbitrary volume,

$$\frac{dC}{dt} + \nabla\cdot\boldsymbol{J} = 0 \tag{23}$$

For an arbitrary, suitably continuous, scalar field, δC, the variational statement (23) reads,

$$\int_\Omega \delta C\left(\frac{dC}{dt} + \nabla\cdot\boldsymbol{J}\right)\,\mathrm{d}V = 0 \tag{24}$$

Rearranging, and making use of the divergence theorem, the weak form renders,

$$\int_\Omega \left[\delta C\left(\frac{dC}{dt}\right) - \boldsymbol{J}\cdot\nabla\delta C\right]\,\mathrm{d}V + \int_{\partial\Omega_q} \delta C q\,\mathrm{d}S = 0 \tag{25}$$

where $q = \boldsymbol{J}\cdot\boldsymbol{n}$ is the concentration flux exiting the body across $\partial\Omega_q$. The diffusion is driven by the gradient of the chemical potential $\nabla\mu$. Accordingly, the mass flux follows a linear Onsager relationship,

$$\boldsymbol{J} = -\frac{DC}{RT}\nabla\mu \tag{26}$$

where D is the diffusion coefficient. The chemical potential of hydrogen in lattice sites is given by,

$$\mu = \mu^0 + RT \ln \frac{\theta_L}{1-\theta_L} - \bar{V}_H \sigma_H \tag{27}$$

Here, μ^0 denotes the chemical potential in the standard case, θ_L the occupancy of lattice sites, and σ_H the hydrostatic stress. The last term corresponds to the so-called stress-dependent part of the chemical potential μ_σ, with $\bar{V}_H$ being the partial molar volume of hydrogen in solid solution. By substituting (27) into (26), and considering the relation between the occupancy and the number of sites, $\theta_L = C/N$, one reaches

$$\boldsymbol{J} = -\frac{DC}{(1-\theta_L)} \left(\frac{\nabla C}{C} - \frac{\nabla N}{N} \right) + \frac{D}{RT} C \bar{V}_H \nabla \sigma_H \tag{28}$$

which, after making the common assumptions of low occupancy ($\theta_L \ll 1$) and constant interstitial sites concentration ($\nabla N = 0$), renders

$$\boldsymbol{J} = -D \nabla C + \frac{D}{RT} C \bar{V}_H \nabla \sigma_H \tag{29}$$

And accordingly, the hydrogen transport equation becomes

$$\int_\Omega \left[\delta C \left(\frac{1}{D} \frac{dC}{dt} \right) + \nabla \delta C \nabla C - \nabla \delta C \left(\frac{\bar{V}_H C}{RT} \nabla \sigma_H \right) \right] \mathrm{d}V = -\frac{1}{D} \int_{\partial \Omega_q} \delta C q \, \mathrm{d}S \tag{30}$$

2.3. Numerical implementation

The finite element (FE) method is used to solve the coupled mechanical-diffusion-phase field problem. Using Voigt notation, the nodal values of the displacements, phase field and hydrogen concentration are interpolated as follows,

$$\boldsymbol{u} = \sum_{i=1}^{m} \boldsymbol{N}_i \boldsymbol{u}_i \,, \qquad \phi = \sum_{i=1}^{m} N_i \phi_i \,, \qquad C = \sum_{i=1}^{m} N_i C_i \tag{31}$$

where m is the number of nodes and $\boldsymbol{N}_i$ are the interpolation matrices - diagonal matrices with the nodal shape functions N_i as components. Accordingly, the corresponding gradient quantities can be discretized by,

$$\boldsymbol{\varepsilon} = \sum_{i=1}^{m} \boldsymbol{B}_i^u \boldsymbol{u}_i \,, \qquad \nabla \phi = \sum_{i=1}^{m} \boldsymbol{B}_i \phi_i \,, \qquad \nabla C = \sum_{i=1}^{m} \boldsymbol{B}_i C_i \tag{32}$$

Here, $\boldsymbol{B}_i$ are vectors with the spatial derivatives of the shape functions and $\boldsymbol{B}_i^u$ denotes the standard strain-displacement matrices.

2.3.1. FE discretization of the deformation-phase field problem

Making use of the finite element discretization outlined above and considering that (13a) must hold for arbitrary values of $\delta \boldsymbol{u}$, the discrete equation corresponding to the equilibrium condition can be expressed as the following residual with respect to the displacement field,

$$\boldsymbol{r}_i^u = \int_\Omega \left[(1-\phi)^2 + k\right] (\boldsymbol{B}_i^u)^T \boldsymbol{\sigma_0} \, \mathrm{d}V - \int_\Omega \boldsymbol{N}_i^T \boldsymbol{b} \, \mathrm{d}V - \int_{\partial\Omega_h} \boldsymbol{N}_i^T \boldsymbol{h} \, \mathrm{d}S \tag{33}$$

Similarly, the out-of-balance force residual with respect to the evolution of the crack phase field is obtained by discretizing (13b),

$$r_i^\phi = \int_\Omega \left[-2(1-\phi) N_i \, H + G_c\,(\theta) \left(\frac{1}{\ell} N_i \, \phi + \ell \boldsymbol{B}_i^T \nabla \phi \right) \right] \mathrm{d}V \tag{34}$$

and the components of the consistent stiffness matrices can be obtained by differentiating the residuals with respect to the incremental nodal variables:

$$\boldsymbol{K}_{ij}^{\boldsymbol{u}} = \frac{\partial \boldsymbol{r}_i^{\boldsymbol{u}}}{\partial \boldsymbol{u}_j} = \int_\Omega \left[(1-\phi)^2 + k\right] (\boldsymbol{B}_i^{\boldsymbol{u}})^T \boldsymbol{C}_0 \boldsymbol{B}_j^{\boldsymbol{u}} \, \mathrm{d}V \tag{35}$$

$$\boldsymbol{K}_{ij}^{\phi} = \frac{\partial r_i^\phi}{\partial \phi_j} = \int_\Omega \left[\left(2H + \frac{G_c\,(\theta)}{\ell} \right) N_i N_j + G_c\,(\theta)\, \ell \boldsymbol{B}_i^T \boldsymbol{B}_j \right] \mathrm{d}V \tag{36}$$

2.3.2. FE discretization of mass transport

A residual vector can be readily obtained by discretizing (30), given that δC indicates an arbitrary virtual variation of the hydrogen concentration:

$$r_i^C = \int_\Omega \left[N_i^T \left(\frac{1}{D} \frac{dC}{dt} \right) + \boldsymbol{B}_i^T \nabla C - \boldsymbol{B}_i^T \left(\frac{\bar{V}_H C}{RT} \nabla \sigma_H \right) \right] \mathrm{d}V + \frac{1}{D} \int_{\partial\Omega_q} N_i^T q \, \mathrm{d}S \tag{37}$$

From which a diffusivity matrix can be defined,

$$\boldsymbol{K}_{ij}^C = \int_\Omega \left(\boldsymbol{B}_i^T \boldsymbol{B}_j - \boldsymbol{B}_i^T \frac{\bar{V}_H}{RT} \nabla \sigma_H N_j \right) \mathrm{d}V \tag{38}$$

where the discretization given in Eq. (31) has also been employed to interpolate the time derivatives of the nodal concentrations. The diffusivity matrix is affected by the gradient of the hydrostatic stress, σ_H, which is computed at the integration points from the nodal displacements, extrapolated to the

nodes by means of the shape functions, and subsequently multiplied by $\boldsymbol{B}$ to compute $\nabla\sigma_H$. Quadratic elements should therefore be employed.

At the same time, one can readily identify a concentration capacity matrix,

$$\boldsymbol{M}_{ij} = \int_\Omega N_i^T \frac{1}{D} N_j \, \mathrm{d}V \tag{39}$$

and a diffusion flux vector,

$$\boldsymbol{F}_i = -\frac{1}{D} \int_{\partial\Omega_q} N_i^T q \, \mathrm{d}S \tag{40}$$

Accordingly, the discretized hydrogen transport equation reads,

$$\boldsymbol{K}^C \boldsymbol{C} + \boldsymbol{M}\dot{\boldsymbol{C}} = \boldsymbol{F} \tag{41}$$

2.3.3. Coupled scheme

The deformation, diffusion and phase field fracture problems are weakly coupled. First, mechanical deformation impacts diffusion through the stress field, governing the pressure dependence of the bulk chemical potential. Secondly, mass transport affects the fracture resistance via hydrogen buildup in the fracture process zone, reducing the critical energy release rate. And thirdly, the hydrogen-sensitive phase field degrades the strain energy density of the solid.

We solve the linearized finite element system,

$$\begin{bmatrix} \boldsymbol{K}^u & 0 & 0 \\ 0 & \boldsymbol{K}^\phi & 0 \\ 0 & 0 & \boldsymbol{K}^C \end{bmatrix} \begin{bmatrix} \boldsymbol{u} \\ \boldsymbol{\phi} \\ \boldsymbol{C} \end{bmatrix} + \begin{bmatrix} 0 & 0 & 0 \\ 0 & 0 & 0 \\ 0 & 0 & \boldsymbol{M} \end{bmatrix} \begin{bmatrix} \dot{\boldsymbol{u}} \\ \dot{\boldsymbol{\phi}} \\ \dot{\boldsymbol{C}} \end{bmatrix} = \begin{bmatrix} \boldsymbol{r}^u \\ \boldsymbol{r}^\phi \\ \boldsymbol{r}^C \end{bmatrix} \tag{42}$$

by means of a time parametrization and an incremental-iterative scheme in conjunction with the Newton-Raphson method. Due to its robustness, and despite requiring a time increment sensitivity analysis, a staggered solution scheme is adopted to solve the deformation-phase field coupling. Integration schemes are discussed at large in the documentation that accompanies the phase field subroutine without hydrogen (see www.empaneda.com/codes).

3. ABAQUS peculiarities and usage instructions

The hydrogen-dependent phase-field model presented is implemented by means of an Abaqus UEL subroutine, which allows for user-defined computation of the element tangent stiffness matrices and the nodal force vectors. We consider isoparametric 2D quadrilateral quadratic elements with 4 degrees of freedom per node, i.e. u_x, u_y, ϕ and C, and four integration points. The extension to a three dimensional case is straightforward.

A number of quantities are stored as solution-dependent state variables `SVARS`, enabling the use of semi-implicit staggered schemes and easing the extension to history-dependent problems (e.g., plasticity). These are shown in Table 2. The stress variables refer to the undamaged stress tensor $\boldsymbol{\sigma}_0$.

Variable	SVARS numbering
Axial stresses - σ_{11} , σ_{22} , σ_{33}	SVARS(1), SVARS(2), SVARS(3)
Shear stress - σ_{12}	SVARS(4)
Axial strains - ϵ_{11} , ϵ_{22} , ϵ_{33}	SVARS(5), SVARS(6), SVARS(7)
Shear strain - ϵ_{12}	SVARS(8)
Crack phase-field - ϕ	SVARS(9)
Hydrostatic stress - σ_H	SVARS(10)
History variable field - H	SVARS(11)

Table 2: List of solution dependent state variables for the UEL.

The use of user element subroutines has the drawback that integration point variables cannot be visualized in Abaqus/Viewer. This limitation is intrinsic to the fact that the only information that Abaqus requests from the UEL subroutine are the stiffness matrix and the right-hand side nodal force vector - the magnitude of the stresses and the strains, as well as the choice of shape functions, is information that is not available as output. To overcome this limitation we here make use of an auxiliary dummy mesh consisting of standard Abaqus elements that resemble the user defined element in terms of number of nodes and integration points (i.e., CPE8R). The material response at each integration point in the auxiliary mesh is defined using a user material subroutine (UMAT), which enables the user to define the constitutive matrix and the stresses from the strain values. In this auxiliary mesh, the

stress components and the constitutive matrix are made equal to zero (i.e., they have no influence in the solution of the global system). The data from our UEL that we want to observe in Abaqus/Viewer is stored in a Fortran module, which allows transferring to the UMAT subroutine. In the UMAT the information is passed to the built-in array `STATEV` for each corresponding element and integration point. If SDV variables are requested as Field Output we would be able to visualize the results. Table 3 shows the equivalence between model variables and SDVs. Here, the stress variables refer to the damaged stress tensor $\boldsymbol{\sigma}$.

Variable	SDVs numbering
Axial stresses - σ_{11} , σ_{22} , σ_{33}	SDV1, SDV2, SDV3
Shear stress - σ_{12}	SDV4
Axial strains - ϵ_{11} , ϵ_{22} , ϵ_{33}	SDV5, SDV6, SDV7
Shear strain - ϵ_{12}	SDV8
Crack phase-field - ϕ	SDV9
Hydrostatic stress - σ_H	SDV10
Hydrogen concentration - C	SDV11

Table 3: List of solution dependent state variables.

3.1. Usage instructions

The first step is to create the model in Abaqus/CAE. The procedure is the same as with standard Abaqus models but one must take into a account a few considerations. First, we will make use of the coupled mechanical-temperature step as it allows us to define initial conditions, run transient and steady-state analysis and impose different convergence criteria (if needed). The hydrogen concentration will occupy the degree of freedom that corresponds to the temperature. Additionally, one should consider the following subtleties:

- The material has to be defined as a user material with 11 solution-dependent variables. (General → Depvar: 11 & General → User Material - Mechanical Constants: 0). Additionally, since we are using the coupled mechanical-temperature step we need to define the density (General → Density) and the specific heat (Thermal → Specific Heat); both are irrelevant in our analysis and are therefore defined equal to 1.

- SDV, Solution dependent state variables, have to be requested as Field Output; as well as displacement, reaction forces, nodal temperature (concentration) and other relevant quantities. (Field Output Request - State/Field/User/Time: SDV, Solution dependent state variables)

- In the Step definition we select the coupled temperature-displacement option, as discussed before. Additionally, we define the incrementation type as "Fixed" (as opposed to "Automatic") to use a constant time increment. This is due to the semi-implicit staggered scheme adopted. In the "Other" category we choose "Ramp linearly over step" as "Default load variation with time"; this is needed to prescribe the displacement boundary condition in the usual manner (varying linearly with Step time). Note that the total step time (in seconds) has a physical meaning in this kind of analysis.

- We define an amplitude to prescribe hydrogen boundary conditions that remain constant throughout the analysis. The amplitude is defined as "Tabular", and in the first line we introduce "Time: 0" and "Amplitude: 1" while in the second line we define "Time: 10000000" (a value that it is at least larger than the total step time) and "Amplitude: 1".

- If we want to prescribe an initial hydrogen concentration throughout the specimen (as is the case in most experiments, where the specimen is pre-charged), we define a predefined field of type temperature. The magnitude of the initial C is then introduced in the units preferred by the user (we use wppm here).

- The mesh has to be very refined in the expected crack propagation area. As discussed in our publication [1], the characteristic element size has to be at least 5 times smaller than ℓ to resolve the fracture process zone. If the crack path is unknown a common strategy is to start with a coarser uniform mesh and refine in subsequent calculations. Use as element type CPE8R.

Once the model has been developed, we create a job and write the input file (Right click on the Job name and click "Write Input"). A few modifications have to be done to the input file to define the user element, the use of a code editor like Notepad++ is recommended. First, we create the dummy visualization mesh. For this purpose we use the Matlab script VirtualMesh.m,

which is part of the Abaqus2Matlab package [18]. Running VirtualMesh.m on the same folder as the input file (Job-1.inp) will create a new file (VisualMesh.inp) with the element connectivity of the visualization mesh.

The first step is to replace the element type,

```
*Element, type=CPE8R
```

with the user element definition,

```
*User element, nodes=8, type=U1, properties=5, coordinates=2, var=44
1,2
1,3
1,11
*ELEMENT, TYPE=U1, ELSET=SOLID
```

where we have defined the number of nodes, the number of properties that will be defined in the input file, the number of coordinates (2D), and the number of `SVARS` (11 per integration point). We have defined the ordering of the DOFs in a way that Eq. (42) corresponds to the element system (as opposed to the node system). Thus, in a 4-node element, the variable `U` contains the components: u_x^1, u_y^1, u_x^2, u_y^2, u_x^3, u_y^3, u_x^4, u_y^4, ϕ^1, ϕ^2, ϕ^3, ϕ^4, C^1, C^2, C^3 and C^4. Accordingly, if one wishes to prescribe a cracked region through the phase field parameter, the boundary condition $\phi = 1$ should be enforced on the DOF 3. Note that DOF 11 is allocated to the hydrogen concentration, as we use for convenience the temperature DOF.

After the element connectivity list one inserts,

```
*UEL PROPERTY, ELSET=SOLID
210000., 0.3 ,0.05, 2.7, 0.0127
*Element, type=CPE8R, elset=Visualization
```

and immediately afterwards the visualization connectivity list (i.e., the content of the file VisualMesh.inp created by the Matlab script). Here, we have defined the user element properties following Table 4. Throughout our model we employ SI (mm) units.

UEL PROPERTY	Description
PROPS(1)	E - Young's modulus [MPa]
PROPS(2)	ν - Poisson's ratio
PROPS(3)	ℓ - Phase field length parameter [mm]
PROPS(4)	G_c - Critical energy release rate [MPa mm]
PROPS(5)	D - Diffusion coefficient [mm^2/s]

Table 4: List of user element properties.

And finally, note that, since we have defined our dummy connectivity list within the element set "Visualization", we need to modify the Section definition,

```
*Solid Section, elset=Set-1, material=Material-1
```

to change the name of the element set,

```
*Solid Section, elset=Visualization, material=Material-1
```

Additionally, one should note that a Fortran module has been defined in the first lines of the subroutine for visualization purposes. One has to be sure that the first dimension of the variable `UserVar` is larger than the total number of elements.

3.2. Representative results

We consider as benchmark the case of a square plate with a horizontal crack placed at the middle point of the left side of the plate. The geometric set-up as well as the boundary conditions are illustrated in Fig. 6. The bottom side is fixed while the top edge is moved vertically. Young's modulus is chosen to be $E = 210000$ MPa, Poisson's ratio $\nu = 0.3$ and critical energy release rate $G_c(0) = 2.7$ MPa mm. The load is applied by prescribing a constant total displacement of $u = 0.01$ mm.

Regarding the hydrogen concentration, we choose to operate with units of wt ppm, and we convert to impurity mole fraction within the code when computing the coverage (21). We prescribe as initial condition a uniform hydrogen distribution through the specimen $C(t = 0) = C_0$, as commonly done in laboratory experiments. And while loading we assume that the outer surfaces of the specimen are in contact with the electrochemical solution. This

means that we impose a constant hydrogen concentration at the boundary, of equal magnitude to the initially prescribed one $C_b = C_0$. We consider a long testing time, $t_f = 1 \times 10^7$ s, so as to allow for hydrogen to redistribute in the fracture process zone. We assume an iron-based material and consequently adopt a hydrogen damage coefficient of $\chi = 0.89$, a partial molar volume of $\bar{V}_H = 2000$ mm^3/mol, and a diffusion coefficient of $D = 0.0127$ mm^2/s. Note that we adopt in the code units of N, mol and mm; thus, the gas constant is given by $R = 8314$ N·mm/(mol·K).

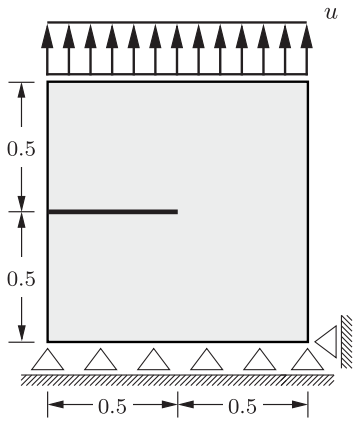

Figure 6: Notched square plate subjected to tension test, geometry and boundary conditions.

Since the goal is to provide an example file, a coarse mesh is adopted to allow for a rapid simulation (the job finishes in minutes); as discrete techniques (see, e.g., [9]), the phase field fracture method requires a refined mesh along the potential crack propagation path to resolve the fracture process zone. A total of 5409 quadrilateral elements are employed, with the characteristic element length along the crack propagation path being equal to $h = 0.005$ mm. We adopt a length scale that is 10 times larger than h to ensure a sufficient number of elements within the process zone, $\ell = 0.05$ mm. To run the calculation type in the command line:

```
abaqus job=Job-1 user=PhaseFieldH.for
```

Linux users may have to change the extension of the subroutine, converting the `PhaseFieldH.for` file to `PhaseFieldH.f`. Optionally, the Python script `ResultsQ8.py` can be used to obtain relevant results in an automated

manner. We show here three representative results: (i) contours of hydrogen concentration, (ii) crack propagation contours, and (iii) force-displacement curves for different hydrogen concentrations. We consider four different environments that range from 1 wt ppm, which corresponds to a 3% NaCl aqueous solution, to testing in air.

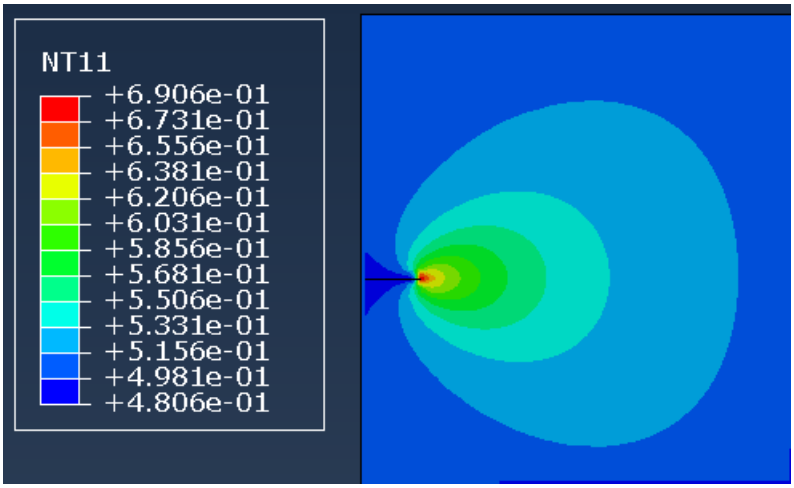

Figure 7: Notched square plate subjected to tension test. Hydrogen concentration in wppm in the fracture process zone at the onset of crack propagation. $C_0 = C_b = 0.5$ wt ppm.

First, Fig. 7 shows how the hydrogen concentration accumulates in the fracture process zone, where hydrostatic stresses are larger. On the other hand, Fig. 8 shows crack propagation contours at different load stages. Blue and red colors correspond to the completely intact and the fully broken state of the material, respectively. The response is not fully symmetric, as the lower bound is fully clamped, and the crack is rather diffuse, as expected given the choice of ℓ.

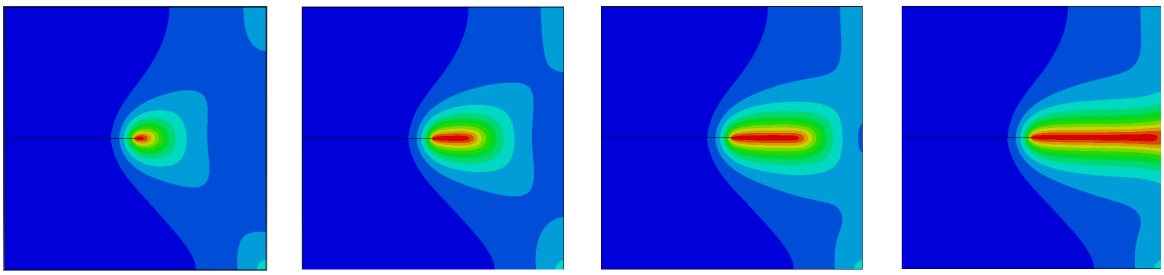

Figure 8: Notched square plate subjected to tension test. Fracture patterns at different load levels for $C_0 = C_b = 0.5$ wt ppm.

Finally, we show in Fig. 9 the load-displacement response as a function of the hydrogen concentration. The figure reproduces the main feature observed in laboratory tests, the load carrying capacity of the specimen reduces with increasing hydrogen concentration. A quantitative agreement with the results of [1] can be adopted by choosing the same value of ℓ, refining the mesh and conducting a time sensitivity analysis (a relatively large time increment is chosen to enable a fast demonstration). As observed in the figure, damage brings in an important drop in the load, with the crack propagating in an unstable manner across the specimen. Computations proceed without convergence problems up until the load has dropped almost completely. Thus, the method is able to model unstable crack propagation without the need of control algorithms [19, 20]. The present benchmark constitutes a rather demanding boundary value problem from the convergence perspective and the main files provided where sufficient to model all the examples of [1] without convergence issues. However, two additional files are provided to the reader for more demanding problems. As discussed in the documentation of the phase field implementation without hydrogen (see www.empaneda.com/codes), convergence can be improved if we store the non-converged values of H_t (referred to as approach D). Additionally, one can run the Explicit/Forward Euler version with equilibrium correction (approach E).

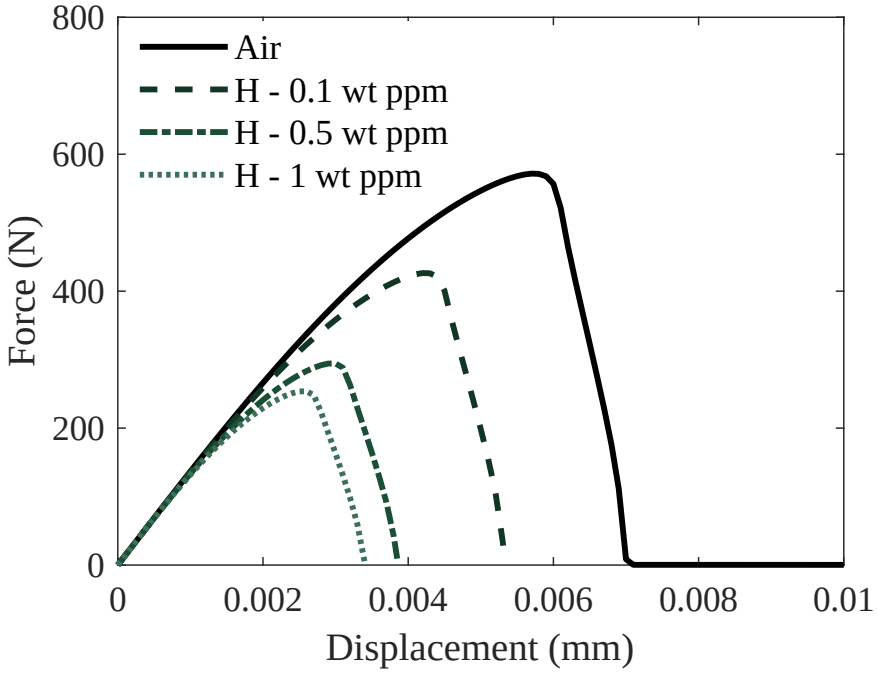

Figure 9: Load-deflection curve obtained in the simple benchmark of a cracked square plate subjected to tension.

In addition to the main subroutine and the input file for this simple boundary value problem, subroutines and input files are provided for other integration schemes (see Appendix A and the discussion on integration schemes in the documentation of the UEL for phase field fracture).

4. Conclusions

We have provided a robust implementation of the coupled deformation - hydrogen diffusion - phase field fracture formulation presented in [1]. The code can easily be extended to incorporate other physical mechanisms. We hope that the present numerical framework can assist in accurately modelling hydrogen assisted fracture of laboratory specimens and industrial components, a complicated and often elusive task.

5. Acknowledgements

E. Martínez-Pañeda also acknowledges financial support from the People Programme (Marie Curie Actions) of the European Union's Seventh Framework Programme (FP7/2007-2013) under REA grant agreement n° 609405 (COFUNDPostdocDTU).

Appendix A. List of files

Main folder

Job-1.inp - Input file for the benchmark problem of a cracked square subjected to tension.

PhaseFieldH.for - UEL Subroutine with the hydrogen-dependent phase field fracture model. 8-node element and semi-implicit integration scheme (2 fields, C).

ResultsQ8.py - Python script to automatically extract the load displacement curve and show contours.

ExtraFiles folder

Job-1.inp - Example of input file as obtained from Abaqus/CAE, to be read by `VisualMesh.m`.

VisualMesh.m - Matlab script from [18] to create the element connectivity list of the visualization mesh.

Job-1d.inp - Input file for semi-implicit (2 fields) case storing non-converged H_t (D), to be used with `PhaseFieldHd.for`.

Job-1e.inp - Input file for the forward Euler case with residual correction (E), to be used with `PhaseFieldHe.for`.

PhaseFieldHd.for - Subroutine for the semi-implicit (2 fi
elds) case storing non-converged H_t (D).

PhaseFieldHe.for - Subroutine for the forward Euler case with residual correction (E).

References

[1] E. Martínez-Pañeda, A. Golahmar, C. F. Niordson, A phase field formulation for hydrogen assisted cracking, Computer Methods in Applied Mechanics and Engineering 342 (2018) 742–761.

[2] G. Francfort, J.-J. Marigo, Revisiting brittle fracture as an energy minimization problem, Journal of the Mechanics and Physics of Solids 46 (8) (1998) 1319–1342.

[3] B. Bourdin, G. A. Francfort, J. J. Marigo, Numerical experiments in revisited brittle fracture, Journal of the Mechanics and Physics of Solids 48 (4) (2000) 797–826.

[4] B. Bourdin, G. A. Francfort, J. J. Marigo, The variational approach to fracture, Springer Netherlands, 2008.

[5] C. Miehe, M. Hofacker, F. Welschinger, A phase field model for rate-independent crack propagation: Robust algorithmic implementation based on operator splits, Computer Methods in Applied Mechanics and Engineering 199 (45-48) (2010) 2765–2778.

[6] M. J. Borden, C. V. Verhoosel, M. A. Scott, T. J. R. Hughes, C. M. Landis, A phase-field description of dynamic brittle fracture, Computer Methods in Applied Mechanics and Engineering 217-220 (May) (2012) 77–95.

[7] M. J. Borden, T. J. R. Hughes, C. M. Landis, C. V. Verhoosel, A higher-order phase-field model for brittle fracture: Formulation and analysis within the isogeometric analysis framework, Computer Methods in Applied Mechanics and Engineering 273 (2014) 100–118.

[8] S. Serebrinsky, E. A. Carter, M. Ortiz, A quantum-mechanically informed continuum model of hydrogen embrittlement, Journal of the Mechanics and Physics of Solids 52 (10) (2004) 2403–2430.

[9] S. del Busto, C. Betegón, E. Martínez-Pañeda, A cohesive zone framework for environmentally assisted fatigue, Engineering Fracture Mechanics 185 (2017) 210–226.

[10] D. E. Jiang, E. A. Carter, Diffusion of interstitial hydrogen into and through bcc Fe from first principles, Physical Review B - Condensed Matter and Materials Physics 70 (6) (2004) 1–9.

[11] A. Chambolle, An approximation result for special functions with bounded deformation, Journal des Mathematiques Pures et Appliquees 83 (7) (2004) 929–954.

[12] G. Bellettini, A. Coscia, Discrete approximation of a free discontinuity problem, Numerical Functional Analysis and Optimization 15 (3-4) (1994) 201–224.

[13] E. Martínez-Pañeda, C. F. Niordson, On fracture in finite strain gradient plasticity, International Journal of Plasticity 80 (2016) 154–167.

[14] E. Martínez-Pañeda, S. Natarajan, S. Bordas, Gradient plasticity crack tip characterization by means of the extended finite element method, Computational Mechanics 59 (5) (2017) 831–842.

[15] D. E. Jiang, E. A. Carter, First principles assessment of ideal fracture energies of materials with mobile impurities: Implications for hydrogen embrittlement of metals, Acta Materialia 52 (16) (2004) 4801–4807.

[16] A. Alvaro, I. Thue Jensen, N. Kheradmand, O. M. Løvvik, V. Olden, Hydrogen embrittlement in nickel, visited by first principles modeling, cohesive zone simulation and nanomechanical testing, International Journal of Hydrogen Energy 40 (47) (2015) 16892–16900.

[17] A. Tehranchi, X. Zhang, G. Lu, W. A. Curtin, Hydrogen vacancy dislocation interactions in α -Fe, Modelling and Simulation in Materials Science and Engineering 25 (2017) 025001 (13 pp).

[18] G. Papazafeiropoulos, M. Muñiz-Calvente, E. Martínez-Pañeda, Abaqus2Matlab: A suitable tool for finite element post-processing, Advances in Engineering Software 105 (2017) 9–16.

[19] J. Segurado, J. LLorca, A new three-dimensional interface finite element to simulate fracture in composites, International Journal of Solids and Structures 41 (11-12) (2004) 2977–2993.

[20] E. Martínez-Pañeda, S. del Busto, C. Betegón, Non-local plasticity effects on notch fracture mechanics, Theoretical and Applied Fracture Mechanics 92 (2017) 276–287.